Vacancy-mediated intermixing in InAs/InP(001) quantum dots subjected to ion implantation

C. Dion,[1,a)] P. Desjardins,[1] F. Schiettekatte,[2] M. Chicoine,[2] M. D. Robertson,[3] N. Shtinkov,[4] P. J. Poole,[5] X. Wu,[5] and S. Raymond[5]

[1]*Regroupement Québécois sur les Matériaux de Pointe (RQMP), Département de Génie Physique, École Polytechnique de Montréal, Montréal, Québec H3C 3A7, Canada*
[2]*Regroupement Québécois sur les Matériaux de Pointe (RQMP), Département de Physique, Université de Montréal, Montréal, Québec H3C 3J7, Canada*
[3]*Department of Physics, Acadia University, Wolfville, Nova Scotia B4P 2R6, Canada*
[4]*Department of Physics, University of Ottawa, Ottawa, Ontario K1N 6N5, Canada*
[5]*Institute for Microstructural Sciences, National Research Council, Ottawa, Ontario K1A 0R6, Canada*

We have investigated the influence of defects emanating from phosphorus implantation damage in the InP capping layer on postgrowth thermally induced intermixing in self-assembled InAs/InP(001) quantum dots (QDs). Photoluminescence (PL) spectra from as-grown samples could be described as the superposition of separate PL peaks where each peak corresponded to emission from an ensemble of QDs with a particular height ranging from 4 to 13 ML. Blueshift of up to 270 meV and significant bandwidth broadening were observed in the PL spectra after ion implantation with a fluence of $5 \times 10^{11} - 10^{14}$ cm^{-2} and subsequent annealing at temperatures ranging from 450 to 600 °C. From the analysis of the evolution of the QD peaks upon intermixing, which revealed the coexistence of intact QD PL and a broad PL feature related to heavily intermixed QDs, it was suggested that the bandwidth broadening resulted from spatial inhomogeneity in the compositional intermixing. In order to better understand the mechanism responsible for the ion-implantation-induced intermixing, samples capped with a stack of compressively strained In$_{0.75}$Ga$_{0.25}$As/InP quantum wells (QWs) were prepared to trap vacancies released by the implantation damage while not inhibiting the effect of the interstitials. Both blueshift and bandwidth broadening were suppressed in samples containing the strained InGaAs QWs, whereas the evolution of the PL spectra from the QDs behaves as expected for interstitial-mediated intermixing. The vacancies were thus believed to be trapped in the QWs and indicated that intermixing in ion-implanted InP capped samples is mediated by vacancies. The shape of the QDs changed from a truncated pyramid in the as-grown state to a double convex lens structure after intermixing as confirmed by cross-sectional scanning transmission electron microscopy imaging. Furthermore, the change in shape and compositional intermixing of the QDs were attributed to vacancy trapping in the vicinity of the QDs as based on atomistic strain calculations. © *2008 American Institute of Physics*. [DOI: 10.1063/1.2970093]

I. INTRODUCTION

Considerable attention has been given to self-assembled InAs/InP quantum dots (QDs) as active elements in tunable lasers for use in the next generation of optical networks and biological imaging systems operating in the 1.5 μm wavelength range.[1–3] The integration of QDs into modern optoelectronic devices is dependent on being able to precisely control their emission wavelength which can be achieved by postgrowth band gap tuning via thermally induced interdiffusion of atoms at the QD/barrier interface. This modifies the confinement potential and hence the energy levels of the heterostructure. The compositional intermixing process is facilitated by the motion of point defects that are either native or intentionally incorporated into specific regions of the sample, for example, by low temperature growth of the cap-

ping layer [grown-in defects (GID)],[4] dielectric capping,[5] or high-energy (low-energy) ion implantation above[6] (through[7]) the emitting layer.

In ion-implanted heterostructures, both interstitial- and vacancy-mediated processes can stimulate compositional intermixing. Given that the evolution of the photoluminescence (PL) characteristics with annealing time and temperature is similar for dielectric capping, GID, and low-energy ion implantation (LEII), it was assumed by several authors that the dominant defects responsible for intermixing in InGaAs/InP quantum wells (QWs) were P interstitials.[4,8] In InAs/InP QDs, intermixing using conventional annealing,[9] laser annealing,[10] dielectric capping,[10–12] and GID[13] generally resulted in a progressive blueshift of the overall QD emission spectra with no significant peak broadening. In sharp contrast, intermixing stimulated by the creation of defects in the capping layer using ion implantation yielded significant bandwidth broadening of the emission spectra.[14,15] Furthermore, the temperature threshold required to induce intermixing in ion-implanted samples was significantly re-

---

duced (~400 °C) as compared to the other techniques mentioned above (~600–725 °C range). These latter results suggest that the dominant defect responsible for intermixing in ion-implanted InAs/InP QDs is different than P interstitials, possibly vacancies which are also created as a result of the ion-implantation damage.

In this work, we used PL spectroscopy and cross-sectional scanning transmission electron microscopy (STEM) to investigate ion-implantation-induced intermixing in InAs/InP QDs. Two series of experiments were performed to elucidate the underlying mechanism. In the first set of experiments, the influence of the annealing temperature, the distance between implantation damage in the InP capping layer and the InAs QDs, and the P implantation fluence on QD PL characteristics was examined. It is shown that the ion-implantation-induced intermixing process is spatially inhomogeneous and characterized by the presence of relatively intact as well as extensively intermixed areas. In order to discriminate the effects of interstitials and vacancies on the intermixing dynamics, a second set of experiments was performed on samples capped with compressively strained InGaAs/InP QWs which were known to trap vacancies emanating from the implanted region.[16,17] From these results, we show that intermixing in ion-implanted InP capped InAs/InP QDs is dominated by the motion of vacancies. In addition, as confirmed using STEM imaging and atomic strain calculations, vacancy trapping also occurs in the compressively strained InAs/InP QDs, which is believed to be the main mechanism responsible for the ion-implantation-induced intermixing observed at a relatively low temperature annealing.

II. EXPERIMENTAL DETAILS

All samples were grown on semi-insulating Fe-doped InP(001) substrates by chemical beam epitaxy from trimethylindium, arsine, and phosphine. The sample used for ion-implantation-induced intermixing experiments consisted of a 128 nm thick InP buffer layer, ~2.2 ML of InAs, followed by a 25 s growth interruption, and a 30 nm thick InP capping layer, all grown at 515 °C. The temperature was then ramped down to 500 °C for the growth of a 790 nm thick InP layer. We have also examined intermixing in a sample containing GID.[13,18] This sample consisted of a 120 nm thick InP buffer layer, ~2.2 ML of InAs, followed by a 35 s growth interruption to allow QD formation, and a 40 nm thick InP capping layer, all grown at 505 °C. The temperature was then ramped down to 450 °C for the growth of a 760 nm thick InP layer which contained a large quantity of GID as compared to samples grown at the standard temperature of ~500 °C. Optimal growth conditions were then used for the growth of a 33 nm thick InGaAs capping layer. More precisely, GID in low temperature grown InP are related to a P-rich stoichiometry with a large quantity of P_{In} antisite defects,[19,20] which upon annealing result in an excess of P interstitials that promote interdiffusion.[21,22]

The samples used for the experiments on vacancy trapping in compressively strained QWs are shown schematically in Figs. 1(a) and 1(b). The sample represented in
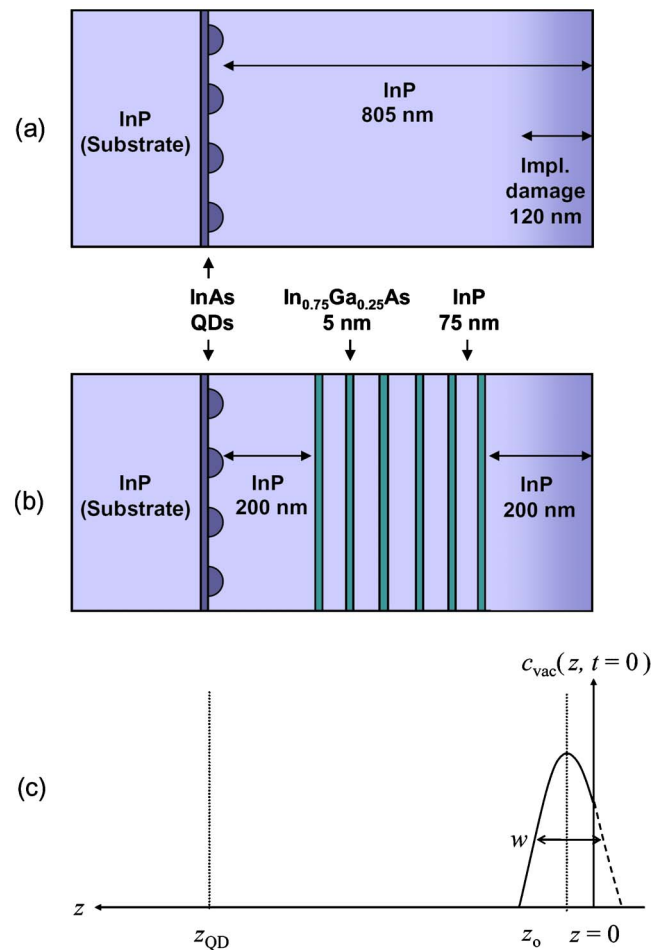

FIG. 1. (Color online) Schematic illustrations of the (a) InP and (b) QW-capped samples, and (c) initial defect concentration profile, $c_{vac}(z, t=0)$, as a function of position z, z_{QD} and z_0 are respectively the QD position and the center position of the distribution relative to the surface.

Fig. 1(a) consisted of a 125 nm thick InP buffer layer, ~2.9 ML InAs QD layer, followed by a 25 s growth interruption, and a 32 nm thick InP capping layer, all grown at 515 °C. The temperature was then ramped down to 500 °C for the growth of a 773 nm thick InP layer so that the total InP capping layer thickness was 805 nm. The sample shown in Fig. 1(b) was similar to that just described, except that a six period stack of 5 nm thick $In_{0.75}Ga_{0.25}As$ QWs with 75 nm InP spacers was inserted in the InP capping layer, 200 nm away from both the surface and the QD plane. The indium concentration and QW thickness were chosen to produce 1.5% of compressive strain while avoiding the creation of dislocations in the heterostructure.[23]

Samples were implanted with phosphorus ions to avoid introducing additional chemical impurities. Implantations were performed at 7° off the (001) direction to minimize channeling effects. The substrate temperature was maintained at 200 °C to prevent surface amorphization[6] and the implantation fluence Φ ranged from 5×10^{11} to 10^{14} cm^{-2}. Based on SRIM 2000 simulations,[24] the energy of P ions was set to 30 keV to confine implantation damage to the first 120 nm below the top surface [see Fig. 1(c)]. In order to examine the influence of the distance between the implanted region and the InAs QDs on the intermixing dynamics,

pieces of the sample containing compressively strained InGaAs/InP QWs were chemically etched before ion implantation so that only 200 nm of InP remained on top of the QD layer. The InGaAs QWs were removed using a $C_6H_8O_7:H_2O_2$ (3:1) solution, while a $HCl:H_3PO_4$ (1:3) solution was used for the etching of the InP.

Samples were subjected to rapid thermal annealing (RTA) using an AG Associates Heatpulse 410 system in a VLSI grade nitrogen atmosphere. In order to prevent excessive loss of group V atoms during annealing, all samples were proximity capped with InP substrates, except for the GID samples which were covered with GaAs. The thermal annealing was performed at temperatures T_a in the 450–750 °C range for times t_a of either 120 or 300 s.

Low temperature (77 K) PL measurements were conducted using the 532 nm line of a Nd:YVO$_4$ laser as the excitation source, except for the GID samples which were probed using the 760 nm line of a Ti:sapphire so that the InGaAs capping layer could be penetrated. In both cases, the incident light power density was kept constant at 50 W cm^{-2} over a 50 μm diameter beam spot that probed approximately 10^5 QDs. The spectra were acquired using a double grating spectrometer and a liquid nitrogen cooled germanium detector. The resolution of the acquisition system was about 4 meV. In order to properly observe the QD emission in the samples containing the InGaAs QWs, the QWs were etched away prior to PL measurement. While the as-grown structures were etched using the solutions described above, intermixed InGaAsP QWs had to be removed using a $H_2SO_4:H_2O_2:H_2O$ (1:1:10) solution due to the highly selective nature of the $C_6H_8O_7:H_2O_2$ (3:1) solution used for InGaAs etching.

Structural investigations of the samples were performed using cross-sectional high-angle annular dark field STEM (HAADF-STEM). The samples were prepared by low-angle polishing using an Allied High Tech Products Inc. MultiPrep™ system, followed by low-angle argon ion milling using a Fischione model 1010 ion mill. Details of the specimen preparation have been previously published.[25,26] HAADF-STEM imaging was performed at 200 kV using a JEOL JEM-2100 F STEM equipped with a Gatan ADF detector (5–11 mm active diameter). The inner detector angle of the ADF detector was set to 51 mrad.

III. EXPERIMENTAL RESULTS

A. Ion-implantation-induced intermixing

PL spectra from as-grown and intermixed InAs/InP QDs subjected to P implantation ($\Phi=10^{14}$ cm^{-2}) and annealing at various temperatures are presented in Fig. 2(a). In order to better highlight the specific effects of ion-implantation-induced intermixing, the PL spectra are compared to those obtained for GID-mediated intermixing [see Fig. 2(b)]. In both sets of experiments, the as-grown samples are characterized by a broad emission, centered near 850 meV, arising from the superposition of up to ten inhomogeneously broadened peaks. These peaks correspond to the fundamental electron−heavy-hole transitions (e1-hh1) of ensembles, or families, of QDs each having the same thickness (h_{QD}) in
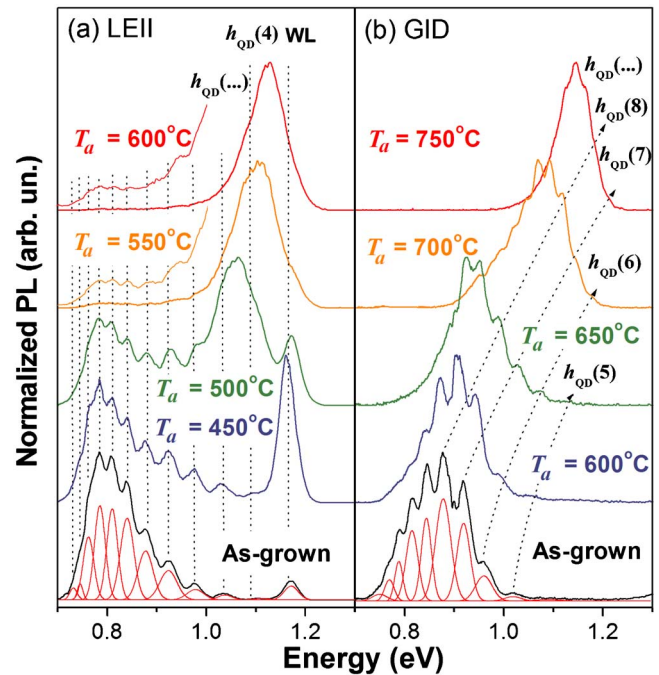

FIG. 2. (Color online) (a) PL spectra at 77 K from as-grown and annealed LEII samples with a fluence of $\Phi=10^{14}$ cm^{-2} as a function of T_a for $t_a=300$ s. (b) PL spectra at 77 K from as-grown and annealed GID samples as a function of temperature T_a for time $t_a=300$ s. A typical example of the peak fitting operation is illustrated for the as-grown samples. Dashed lines illustrate the evolution of the various QD emission peaks, where the numeral in $h_{QD}(i)$ refers to the QD ensemble thickness in terms of an integer number of monolayers. Fine lines in (a) are magnifications of the spectra in that energy range.

terms of an integer number of monolayers.[27,28] The low-intensity peak observed at 1160 meV in Fig. 2(a) can be attributed to the emission from the wetting layer (WL).[29] The relative intensities of the QD peaks and the WL are indicators of the island thickness distribution and QD density, which can vary slightly from one sample to another depending on the growth conditions.[30] For instance, the appearance of a WL peak in the GID sample can probably be attributed to a lower density of QDs.[30] As discussed in Ref. 28, tight-binding calculations were combined with PL results in order to determine the height and P concentration of each QD family in their as-grown state. We have found that the optical transitions from both as-grown LEII and GID samples presented in Fig. 2 arise from 5 to 13 ML thick QDs with an average P composition of $[P]=9.3\pm0.7\%$. This indicates that both samples are structurally similar, a necessary condition for comparison of their properties after different intermixing treatments.

Despite their similarities in the as-grown state, the LEII and GID samples display very different PL behavior after annealing. As shown in Fig. 2(b), the overall QD emission spectra from the GID samples exhibit a progressive blueshift without bandwidth broadening. No significant change in the overall peak shape and width is observed for T_a of up to 700 °C. After annealing at 750 °C, the maximum intensity of the PL spectrum is located at ~1.1 eV and the peak becomes narrower with less resolved subpeaks. This results suggest that the thinner QDs progressively dissolve into the

WL to form a highly disordered QW.[13] In contrast, as shown in Fig. 2(a), no progressive blueshift of the PL spectra is observed from LEII samples upon annealing; however, at comparatively much lower annealing temperatures, a high-energy peak emerges over the original QD emission spectrum. In addition, substantial bandwidth broadening of the PL spectra is observed. After annealing at 600 °C, the PL spectrum becomes dominated by a wide emission peak located at ~1.1 eV that can be attributed to the emission from heavily intermixed QDs. The sudden rise of this high-energy peak, without going through intermediate energy values, suggests that QDs experienced significant and rapid compositional interdiffusion.[14]

In order to quantify the evolution of the PL spectra due to intermixing, all spectra presented in Fig. 2 were analyzed using a multiparameter fit assuming a single Gaussian curve per QD family peak. As a starting point, the initial peak positions for the as-grown samples were estimated based on a previous work.[28] The full widths at half maximum (FWHM) of the peaks—which are related to inhomogeneous broadening within a given family due to small variations in lateral size, composition, electronic environment, or from roughness in the thickness[27]—were constrained to increase with emission energy since interfacial roughness is expected to cause larger relative changes in the confinement emission energy in thinner QDs.[31] The results of this fitting procedure are illustrated in Figs. 2(a) and 2(b) for the as-grown state where the peaks are labeled in terms of h_{QD}. The peak energies obtained for the as-grown samples were then used to initialize the fit of the spectra from annealed samples. In order to quantify the progressive blueshift of individual QD family peaks in the GID samples [Fig. 2(b)], a uniform shift was first applied to all as-grown transition energies and individual peak positions and FWHM were then fit to obtain the best match to each spectrum. For the LEII samples, no progressive blueshift of the QD peaks is observed upon annealing in Fig. 2(a). In this case, the evolution of PL spectra is explained by changes in the relative intensities of the individual peaks. Indeed, as indicated by the dotted line in Fig. 2(a), the QD peaks appear to remain at their initial energies. A significant reduction in the PL intensity of the low-energy peaks associated with thicker QDs is accompanied by the sudden rise of a broad high-energy PL peak with energy corresponding to that of thinner QDs and heavily intermixed QDs. In such samples, the best fits were obtained by keeping the QD peak position energies constant while allowing variations in their amplitude and FWHM. The fitting procedures for the LEII and GID samples were not interchangeable since some QD peaks from the annealed GID samples were found to be located at intermediate energy values, between the two as-grown states. Similarly, it was not possible to attribute the sudden rise of the high-energy peak in PL spectra from annealed LEII samples to a progressive energy shift. In all cases, the fitting procedure allows the determination of the peak energy and FHWM within ±5 meV.

The results of the fitting procedure (peak position and FWHM of each QD peak) are presented in Figs. 3(a) and 3(b) for the GID samples. In Fig. 3(a), the peaks attributed to different QD ensembles shift at similar rates with annealing,
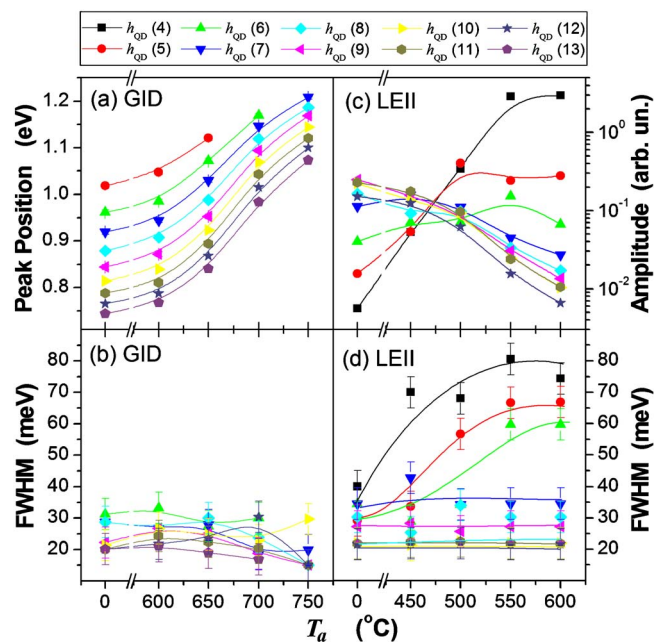

FIG. 3. (Color online) Evolution of the QD emission peaks as a function of annealing temperature T_a. In (a) and (b) are the evolution of the peak position and FWHM, respectively, for GID samples. In (c) and (d) are presented the evolution of the peak amplitude and FWHM, respectively, for LEII samples. The symbols correspond to the various QD ensembles with differing thickness.

as observed in previous publications.[13,18] No evidence of peak broadening with annealing can be seen in Fig. 3(b) where the FWHM remains comparable, within uncertainty, to that in the as-grown state. Consequently, the combination of similar energy shifts and fairly constant FWHM for all QD ensembles results in a relatively constant overall emission bandwidth upon intermixing. Hence, all QDs underwent a similar degree of intermixing, meaning that intermixing in the GID samples was relatively spatially uniform.

The amplitude and FWHM of each peak in the PL spectra are presented in Figs. 3(c) and 3(d) as a function of annealing temperature for LEII samples. The amplitude [Fig. 3(c)] of the emission peaks attributed to QD ensembles with 4, 5, and 6 ML in thickness increase by up to two orders of magnitude after annealing. Since the sudden appearance of a higher density of small QDs is physically unlikely and that the energies associated with heavily intermixed structures of all size in the 0.95–1.15 eV range are similar to those for 4−6 ML thick as-grown QDs, an increase in the population of heavily intermixed structures is believed to have occurred. In addition, the FWHM of these peaks increase from 40 meV in the as-grown state to 80 meV after annealing at 600 °C. This is consistent with the fact that emission in that energy range arises from a heavily disordered system composed of QDs of different sizes and compositions. On the other hand, the emission peaks from QD ensembles of more than 7 ML decrease in amplitude by one order of magnitude, while their FWHM remains constant. This indicates that these emission peaks arise from intact QDs, where many of the QDs previously emitting of this region of the spectrum have now heavily intermixed and contribute to the emission of the broad spectral feature in the region of 0.95−1.15 eV.
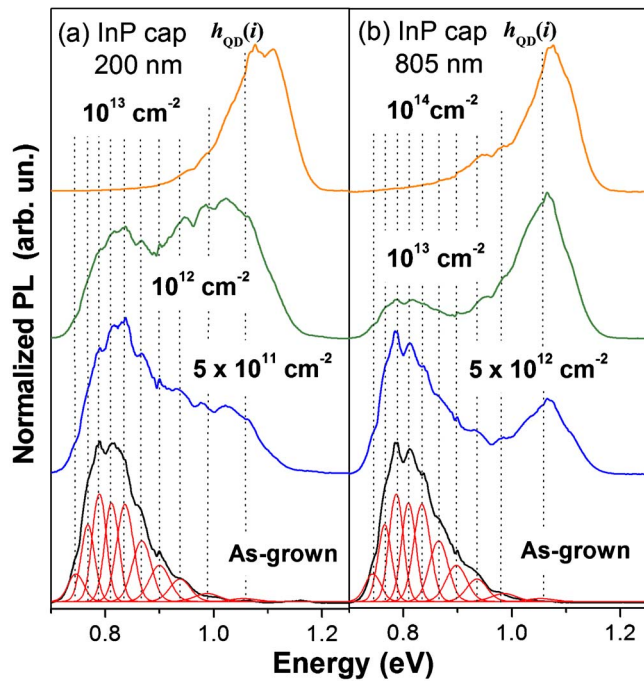
FIG. 4. (Color online) PL spectra at 77 K from intermixed QD samples capped with (a) 200 nm and (b) 805 nm thick InP as a function of implantation fluence Φ for annealing temperature $T_a = 575\,°C$ and time $t_a = 120\,°C$. PL spectra at 77 K from as-grown QDs are also shown for comparison. Results of the peak fitting operation are illustrated for as-grown samples. Dashed vertical lines indicate the peak position of the various QD ensembles.

Altogether, the above results demonstrate that the PL spectra originate from a superposition of multiple emission peaks from both as-grown and heavily intermixed structures. The coexistence of nonintermixed and heavily intermixed QDs within the probed region (about 50 μm in diameter) suggests that intermixing is spatially nonuniform throughout the sample.

The peculiar PL progression with annealing temperature observed in Fig. 2(a) is a general behavior in all of the LEII samples investigated, independent of the P implantation fluence and of the distance between the implanted zone and the InAs QDs. This effect is illustrated in the PL spectra obtained from samples capped with (a) 200 nm and (b) 805 nm thick InP as a function of implantation fluence for $T_a = 575\,°C$, as shown in Fig. 4. Similar to the PL spectra shown Fig. 2, ion-implantation-induced intermixing leads to a reduction in the relative intensity of the low-energy peaks associated with thicker QDs together with an increase in the relative intensity of the high-energy peaks attributed to the thinner and heavily intermixed QDs. This leads to an apparent overall blueshift with significant bandwidth broadening. Comparing the results between the samples with 200 and 805 nm InP caps reveals that the ion fluences required to achieve similar PL characteristics differ by about one order of magnitude. As will be discussed in Sec. IV, this important result provides insights into the transport dynamics of defects, from their creation location in the InP capping layer to the active InAs QD region.

The results presented in Figs. 2(a) and 4, together with other published data (see, for example, Refs. 14 and 15),

indicate that the observed overall PL evolution is common to all ion-implanted InAs/InP QDs even though the changes in the relative intensities between the low- and high-energy peaks are a strong function of annealing and implantation conditions. This behavior is significantly different from that obtained using other intermixing techniques such as GID as shown in Fig. 2(b). Since the motion of P interstitials had been previously proposed to explain GID-induced intermixing,[13] it is reasonable to formulate the hypothesis that the ion-implantation-induced intermixing originates from the presence of vacancies which were also released from the implanted region of the sample.

B. Vacancy trapping in compressively strained InGaAs/InP QWs

The samples shown schematically in Figs. 1(a) and 1(b) were used to discriminate the effects of vacancies and interstitials on intermixing. In Fig. 1(b), the compressively strained InGaAs/InP QWs were used to trap vacancies while not inhibiting the effects of the interstitials.[16,17] Indeed, in a system containing a nonuniform stress field, diffusing particles experience a force in the direction that reduces their interaction energy with the stress field.[32,33] As vacancies in a host crystal create local tensile stresses, the system favors the propagation of these defects toward the compressively strained regions of the sample. Furthermore, because it requires more energy for vacancies to return to the lattice matched regions, these defects are likely to be trapped within the compressively strained layers.[16] On the other hand, interstitials cause local compressive stresses and hence these defects will diffuse away from the compressively strained regions.[16]

The evolution of the QDs PL characteristics from samples with and without the compressively strained InGaAs/InP QWs after implantation with 10^{14} P cm^{-2} and 120 s anneals at T_a ranging from 575 to 725 °C are compared in Fig. 5(a). Implanted InP capped samples are characterized by pronounced intermixing as the QD emission evolves to essentially become a high-energy peak centered at about 1.1 eV, similar to the results presented in Figs. 2(a) and 4. In sharp contrast, the PL spectra from the sample comprising the strained QWs exhibit a slower progressive blueshift of up to 110 meV after annealing at 725 °C with no significant change in the overall peak shape and width. No significant blueshift was measured in an unimplanted reference sample annealed under the same conditions, as highlighted by the dotted spectra in Fig. 5(a).

Comparing the results in Fig. 5(a) with those in Fig. 2(b) reveals that the PL evolution from implanted and annealed QW-capped samples is similar to that observed in samples containing GID, in which intermixing is known to be mediated by the motion of interstitials.[4,13] Since drastic intermixing is suppressed in the presence of the compressive QWs, we attribute the origin of the significant and peculiar intermixing observed in implanted and annealed InP capped samples to the motion of vacancies created by the ion-induced damage.

As mentioned in Sec. II, the QD PL spectra presented in Fig. 5(a) from samples capped with a stack of compressively
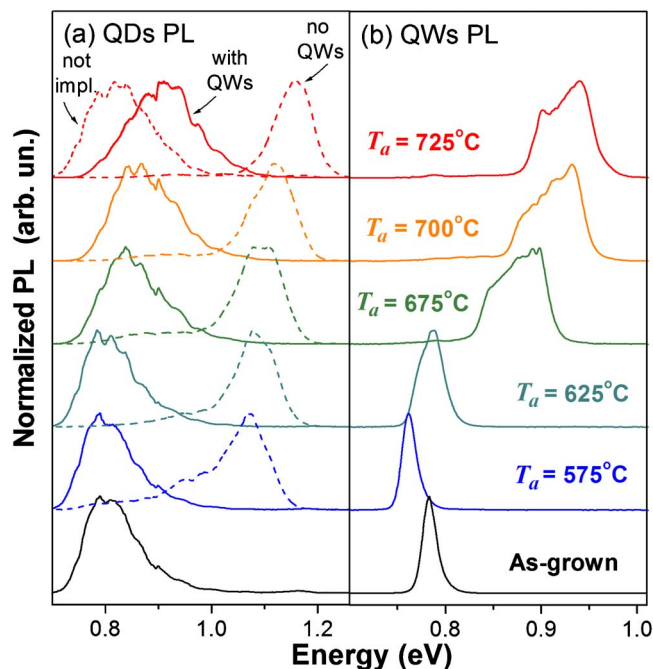
FIG. 5. (Color online) (a) PL spectra at 77 K from as-grown and intermixed ($\Phi = 10^{14}$ cm^{-2}; $T_a = 575-725$ °C, $t_a = 120$ s) QDs in samples capped with pure InP (dashed lines) and a stack of compressively strained In$_{0.75}$Ga$_{0.25}$As/InP QWs (solid lines). PL spectrum at 77 K from an unimplanted InP capped sample (dotted line) annealed at $T_a = 725$ °C for $t_a = 120$ s is also shown for comparison. (b) PL spectra at 77 K from as-grown and intermixed ($\Phi = 10^{14}$ cm^{-2}; $T_a = 575-725$ °C, $t_a = 120$ s) In$_{0.75}$Ga$_{0.25}$As QWs prior to wet chemical etching.

strained QWs were obtained after carefully etching away the QWs after ion implantation and annealing in order to eliminate emission from the QWs. Nevertheless, the QW emission characteristics from unetched samples presented in Fig. 5(b) provide insights into the intermixing dynamics within the strained QW stack. Spectra from as-grown InGaAs QWs are characterized by a single emission peak centered at around 780 meV corresponding to the e1-hh1 transition.[34] Although not explicitly shown here, QW PL peaks from unimplanted samples experience no significant shift for T_a below 750 °C.[35,36] On the other hand, QW PL spectra from implanted and annealed samples exhibit a redshift of about 20 meV after 120 s anneals at T_a below 575 °C and a blueshift up to about 160 meV for $T_a = 725$ °C. Similar PL characteristics were observed by Nie *et al.*[37] from InGaAsP/InP QWs subjected to ion implantation by plasma immersion and RTA. These authors, together with Micallef *et al.*,[38] have shown theoretically that both red- and blueshifts can be attributed to interdiffusion at the InGaAsP/InP interfaces with the sign of the emission shift depending upon the predominance of either group III (redshift) or group V (blueshift) atomic interdiffusion. In addition, the PL spectra displayed in Fig. 5(b) show significant bandwidth broadening, suggesting that the numerous QWs undergo different degrees of intermixing. This observation is consistent with the fact that defects promoting intermixing are emanating from the implanted region on the top surface and that their concentration decreases for QWs located deeper into the structure. This is also in agreement with vacancy trapping in the compres-
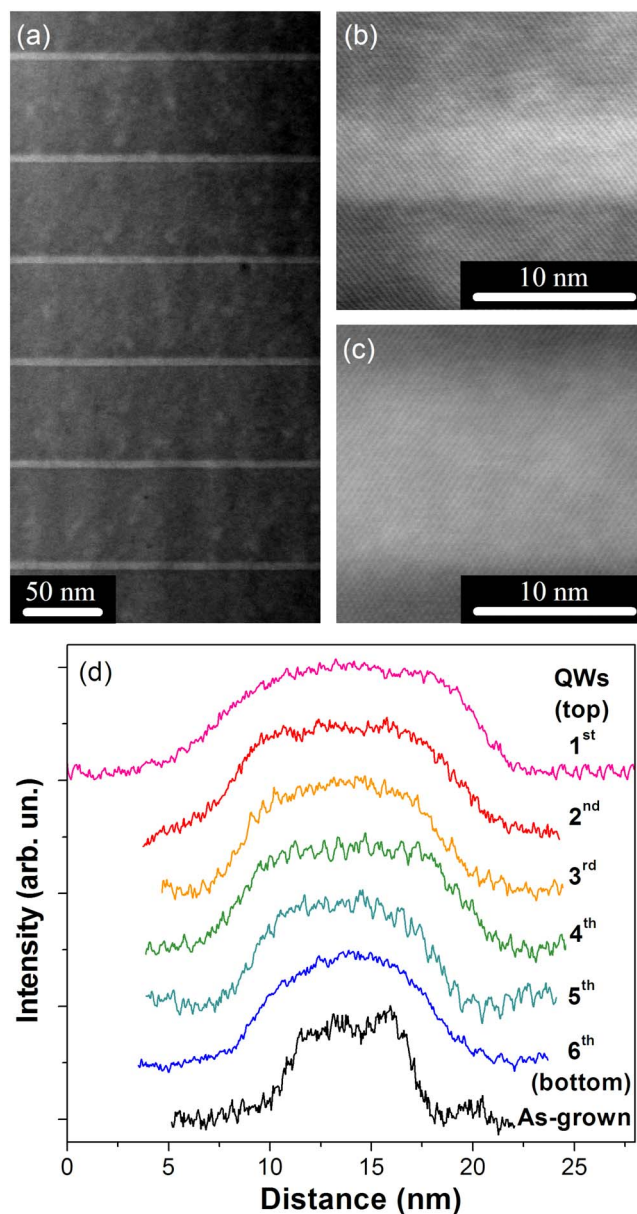

FIG. 6. (Color online) (a) Cross-sectional HAADF-STEM images of the as-grown QW stack. Higher magnification images of the first QW relative to the surface (b) prior to treatment and (c) after intermixing ($\Phi = 10^{14}$ cm^{-2}; $T_a = 725$ °C, $t_a = 120$ s). (d) Line scan profiles across the intermixed QWs ($\Phi = 10^{14}$ cm^{-2}; $T_a = 575-725$ °C, $t_a = 120$ s). A typical profile of an as-grown QW is also shown as a reference.

sively strained QWs as the structures located nearer to the surface can be expected to trap the largest number of vacancies.

As PL results are only indirect evidence of intermixing, STEM investigations were used to confirm that various QWs exhibit progressively decreasing degrees of intermixing as vacancy diffusion progresses deeper into the sample. A typical cross-sectional image of the entire QW stack is shown in Fig. 6(a) while Figs. 6(b) and 6(c) are higher magnification images of the first QW (relative to the top surface) in the as-grown state and after intermixing ($\Phi = 10^{14}$ cm^{-2}, $T_a = 725$ °C, and $t_a = 120$ s). Line scan profiles of the image intensity from every QW after intermixing, averaged over five measurements from different locations in the high mag-
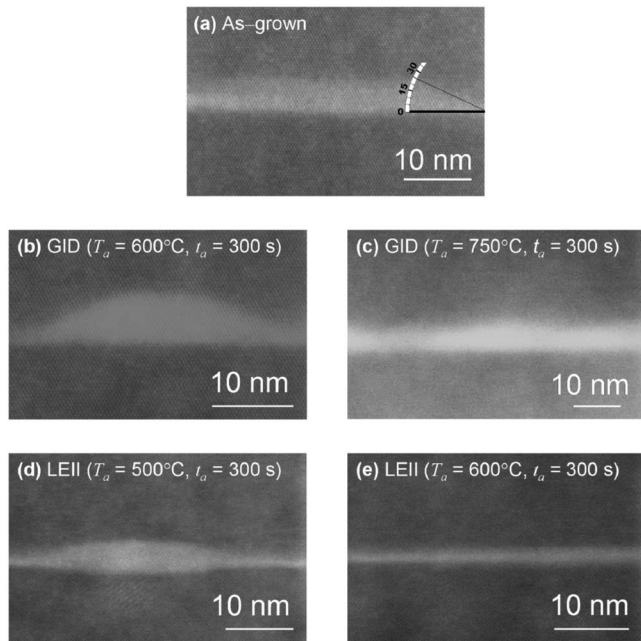
FIG. 7. (a) Cross-sectional HAADF-STEM images ([110] zone axis) of a typical as-grown QD. Images of typical structures in GID samples after annealing for t_a=300 s at (b) T_a=600 °C and (c) T_a=750 °C. Images of typical structures in LEII samples with a fluence of Φ=10^{14} cm^{-2} after annealing for t_a=300 s at (d) T_a=500 °C and (e) T_a=600 °C.

FIG. 8. (Color online) Calculated hydrostatic strain distribution in the [001] plane of a 6 ML thick pure InAs truncated pyramid with (113) side facets on a 2 ML thick InAs WL buried in pure InP matrix. In the color scale, red and blue correspond to compressive and tensile strains, respectively.

nification images, are presented in Fig. 6(d). In addition, a typical profile from an as-grown QW is shown for comparison. The degree of compositional intermixing is largest for QW closer to the surface, thereby corroborating the PL results which showed that the QWs undergo different degrees of intermixing based on their location.

In summary, through the use of a specially designed structure containing compressively strained InGaAs QWs in the InP capping layer to trap vacancies, we have demonstrated that vacancies are the main agent driving compositional intermixing in ion-implanted InP capped InAs/InP QDs. This conclusion has major consequences on the understanding of vacancy-mediated intermixing within InAs/InP QDs. Indeed, since InAs/InP QDs are compressively strained structures, they should also attract vacancies into their vicinity. This latter point is addressed in Sec. III C.

C. Vacancy trapping in compressively strained InAs/InP QDs

In order to examine the possibility of vacancy trapping in compressively strained InAs/InP QD structures, we have investigated the evolution of QD shapes with the degree of intermixing using STEM. The results for the LEII and GID samples were compared to highlight the specific effects of ion-implantation-induced intermixing. Samples exhibiting maximum and intermediate changes in PL in Fig. 2, i.e., GID samples annealed at T_a=750 and 600 °C for t_a=300 s, and LEII samples with fluence Φ=10^{14} cm^{-2} annealed at T_a=600 and 500 °C for t_a=300 s, were selected for these measurements. Typical QD shapes for the various processing conditions are presented in Fig. 7 for (a) as-grown, [(b) and (c)] annealed GID, and [(d) and (e)] annealed LEII samples.
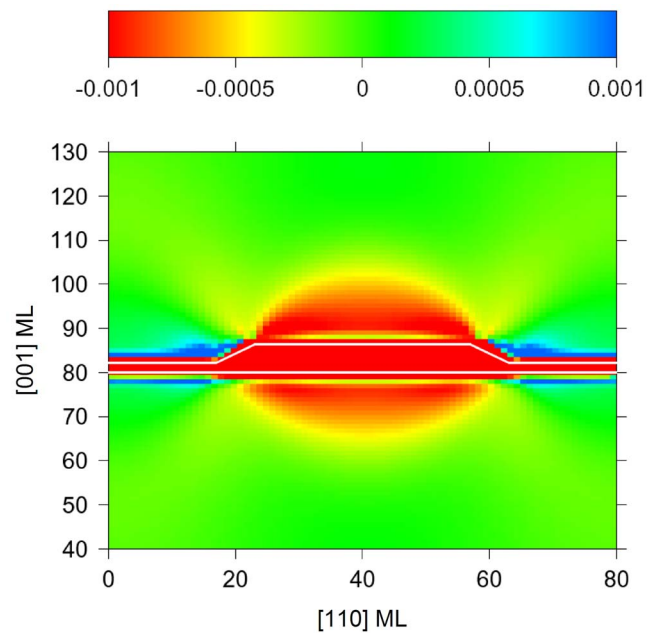
The as-grown InAs/InP QDs [Fig. 7(a)] are truncated pyramids with flat top and bottom surfaces and 25° side angles, corresponding to (113) facets, in agreement with previous reports.[26,39,40] Substantial modifications in the QD shape are observed in samples showing intermediate PL changes. For interstitial-mediated intermixing in GID samples the flat top becomes spherical, transforming the truncated pyramid QD into a domelike structure as shown in Fig. 7(b). On the other hand, vacancy induced intermixing in the LEII samples alters both the top and bottom QD interfaces, creating a double convex lens as displayed in Fig. 7(d). Although the diameter and the thickness of the QDs varied significantly for observations made in different regions of the samples, these general QD shapes were consistently observed. Finally, for samples showing maximum PL changes, Figs. 7(c) and 7(e) show broadened QWs, confirming the dissolution of a vast number of QDs into the WL. No distinct QD structures were found in these samples. This is consistent with the PL results displayed in Figs. 2(a) and 2(b) where both samples are characterized by a much broadened PL peak centered at around 1.1 eV.

Although interstitials and vacancies both lead to broadened QW after significant intermixing, the nature of the defects promoting interdiffusion greatly affects the QD shape in their intermediate intermixed states. Since strain affects the diffusion dynamics of the defects, we have examined this point in more detail using atomistic strain simulations similar to those presented in Ref. 40 using Keating's valence force field method[41] with the parameters reported by Martins and Zunger.[42] The calculated hydrostatic strain distribution in the [001] plane of a 6 ML thick pure InAs truncated pyramid with (113) side facets on a 2 ML thick InAs WL buried in pure InP matrix is presented in Fig. 8. The strain, expressed as a percentage, has been associated to a color scale, where

negative (compressive) and positive (tensile) strains refer to red and blue, respectively. The scale limits were fixed to −0.1% and 0.1% to clearly illustrate small strain variations in the InP matrix. In the scale range displayed, the strain distribution within the QD and WL appears homogeneous, although the actual strain values varied slightly between −3.3% and −2.9%. There is a significant level of compressive strain in the surrounding InP barrier material at the bottom and the top of the pyramidal island. Strain values in these regions are on the order of −0.1% and the compressive strain values gradually diminish away from the QD structure. In contrast, regions around the periphery of the island are under tensile strain up to 0.3%, which quickly decrease away from the QD structure. Similar strain distributions were reported in the literature for InAs QDs embedded in GaAs matrix.[43,44]

Defects traveling down from the top surface of the sample are subjected to the compressive and tensile strain fields around the QD. While interstitials are favorably directed toward the island periphery, the migration of vacancies toward the QDs is energetically favored. Thus, in interstitial-mediated intermixing, QD interdiffusion is expected to proceed mostly along the side interfaces, producing graded QD edges. This is consistent with STEM images from the GID sample displayed in Fig. 7(b). On the other hand, in vacancy-mediated intermixing, the compressive strain accumulation around the base and top surface of the QD should confine the mobile vacancies promoting interdiffusion in these regions. This is in good agreement with the double convex lens shape of QDs after ion-implantation-induced intermixing presented in Fig. 7(d).

The nature of the defects driving interdiffusion in InAs/InP QDs does not only influence the evolution of the QD shape upon intermixing but also has an impact on the interdiffusion dynamics. Since vacancies are confined in the vicinity of the QDs, a single vacancy is expected to induce numerous P–As substitutions at the InAs/InP heterojunction and should therefore produce significantly more intermixing than a single interstitial which is rapidly ejected away from the strained region.[16] Consequently, the P–As substitution coefficient at a given T_a is expected to be much larger when it is promoted by vacancies than when it is controlled by the motion of interstitials. This is consistent with the lower T_a threshold for intermixing observed in Fig. 2. In addition, since a small number of vacancies are required to produce a large level of interdiffusion, this process should be strongly influenced by the probability of the presence of a single vacancy in a single QD. Therefore, it is expected that there will be a coexistence of both intact and intermixed QDs within the sample, which is consistent with the spatial inhomogeneity of ion-implantation-induced intermixing as observed in Sec. III A.

IV. DISCUSSION

In order to gain further insight into the dynamics of vacancy diffusion, we have conducted a quantitative analysis of the results displayed in Fig. 4 which highlights InAs/InP QD samples with 200 and 805 nm thick InP capping layers with

comparable PL characteristics for implantation fluences differing by about one order of magnitude. Based on these observations, we may assume that both experimental conditions led to comparable intermixing diffusion lengths. Furthermore, assuming that atomic interdiffusion in the vicinity of the QDs was governed by a sole diffusion species—vacancies based on the results presented in Sec. III B—the diffusion length of intermixing L_I after a given annealing time t_a can be written as[4,33,45]

$$L_I^2 = \frac{4D^{(\text{P–As})}}{n_0} \int_0^{t_a} c_{\text{vac}}(z_{\text{QD}}, t) dt, \tag{1}$$

where $D^{(\text{P–As})}$ is the P–As substitution coefficient at the QD boundary and $c_{\text{vac}}(z_{\text{QD}}, t)/n_0$ is the concentration of vacancies at the QD position z_{QD} as a function of time t with respect to the total concentration of vacancy sites available n_0. Since both samples were subjected to 120 s anneals at a temperature of 575 °C, it can be reasonably assumed that values of $D^{(\text{P–As})}$ are the same in both conditions. This assumption is valid provided that $D^{(\text{P–As})}$ is not concentration dependent, a reasonable hypothesis for InAs/InP QDs.[18] Thus, based on Eq. (1), both experimental conditions must lead to the same time-integrated $c_{\text{vac}}(z_{\text{QD}}, t)$ value.

Since the concentration of P vacancies (V_P) released by the ion-induced damage is believed to be much larger that the concentration of native defects in thermal equilibrium, vacancies are expected to dominate intermixing dynamics. Under these assumptions, we can estimate the diffusion coefficient associated with the transport of vacancies from their creation location in the InP capping layer to the InAs active region. The initial P vacancy concentration profile $c_{\text{vac}}(z, t=0)$ resulting from ion implantation can be reasonably well described by a Gaussian distribution[24]

$$c_{\text{vac}}(z, t=0) = \frac{A\Phi}{w\sqrt{2\pi}} \exp\left[-\frac{1}{2}\left(\frac{z - z_0}{w} \right)^2 \right], \tag{2}$$

where A, w, and z_0 are the amplitude, the width, and the center position of the Gaussian distribution, respectively [see Fig. 1(c)]. Using the local-source solution of Fick's diffusion equation and the method of superposition[33] with initial conditions given by Eq. (2), the vacancy diffusion concentration profile $c_{\text{vac}}(z, t)$ can be written as

$$c_{\text{vac}}(z, t) = \frac{A\Phi}{w\sqrt{4\pi a D^{(\text{vac-InP})} t}} \exp\left(\frac{-\gamma}{2} \right)$$
$$\times \exp\left(\frac{b^2}{4a} \right) \left[1 - \text{erf}\left(\frac{b}{2\sqrt{a}} \right) \right], \tag{3}$$

where $D^{(\text{vac-InP})}$ is the diffusion coefficient for the transport of vacancies in the InP matrix. In Eq. (3), the constants a, b, and γ are respectively defined as $a = (1/2w^2 + 1/4D^{(\text{vac-InP})}t)$, $b = (z_0/w^2 + 2z/4D^{(\text{vac-InP})}t)$, and $\gamma = (z_0^2/w^2 + 2z^2/4D^{(\text{vac-InP})}t)$.

The integral of Eq. (1) was evaluated numerically over the annealing time $t_a = 120$ s using the vacancy diffusion concentration profile given by Eq. (3). The Gaussian distribution parameters used in Eq. (3) were obtained from SRIM 2000 simulations.[24] Using our experimental conditions (nature of the target, mass, energy, and angle of incidence of the
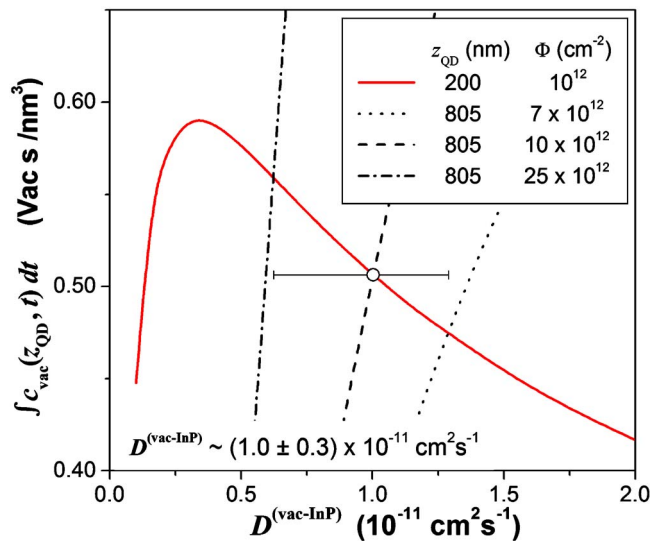
FIG. 9. (Color online) Time integrated vacancy concentration at the QD layer as a function of $D^{(vac\text{-}InP)}$ calculated for $z_{QD} = 200$ nm with $\Phi = 10^{12}$ cm^{-2} (solid line). These results are compared to those obtained for $z_{QD} = 805$ nm with $\Phi = 7 \times 10^{12}$ cm^{-2} (dotted line), 10×10^{12} cm^{-2} (dashed line), and 25×10^{12} cm^{-2} (dashed and dotted line).

ions), these parameters were found to be $A = 243$ V_P/ion, $w = 23.3$ nm, and $z_0 = 22.2$ nm. The results of the integral of Eq. (1) are presented in Fig. 9 as a function of the unknown parameter $D^{(vac\text{-}InP)}$ for $z_{QD} = 200$ and 805 nm with $\Phi = 10^{12}$ and 10^{13} cm^{-2}, respectively, which are the experimental parameters producing similar PL characteristics as observed in Fig. 4. As mentioned above, in order to yield the same intermixing length L_I, both experimental conditions must have the same time-integrated $c_{vac}(z_{QD}, t)$ value. This situation corresponds to the point where both curves shown in Fig. 9 intersect, i.e., for $D^{(vac\text{-}InP)} \sim 10^{-11}$ cm^2 s^{-1}.

Although the comparison between PL spectra from both samples is only semiquantitative, it nevertheless reveals that the fluence ratio to achieve comparable PL characteristics is neither lower than 7 nor higher than 25. We have recalculated the time-integrated $c_{vac}(z_{QD}, t)$ using these latter conditions and plotted the results in Fig. 9. Using these curves, the uncertainty on $D^{(vac\text{-}InP)}$ is found to be of the order of 0.3×10^{-11} cm^2 s^{-1}. In addition, the A value provided by SRIM simulations needs to be treated with caution as it is well-known that this is only an estimate and can easily be off by an order of magnitude. Indeed, it gives a very crude description of damage, assuming Frenkel pairs rather than the damage clusters predicted, for instance, by molecular dynamics and does not include dynamic annealing effects. Still, assuming a displacement energy of 8 eV,[46] SRIM simulations yield $A = 764$ V_P/ion, $w = 23.2$ nm, and $z_o = 21.7$ nm. Besides, since both samples were exposed to the same damage and that the determination of $D^{(vac\text{-}InP)}$ only requires comparison of time-integrated $c_{vac}(z_{QD}, t)$ on a relative scale, such uncertainty has little effect on the value of $D^{(vac\text{-}InP)}$ deduced from our analysis. In fact, when using the parameters obtained for a displacement energy of 5 eV in the calculations, the same value for $D^{(vac\text{-}InP)}$ was found. Therefore, for $T_a = 575$ °C, a diffusion coefficient associated with the transport of vacancies in the InP matrix of

$D^{(vac\text{-}InP)} = (1.0 \pm 0.3) \times 10^{-11}$ cm^2 s^{-1} appears to provide a reasonable estimate. This latter value is two orders of magnitude larger than the diffusion coefficient for the transport of P interstitials in InP at 575 °C, which is $\sim 10^{-13}$ cm^2 s^{-1}.[18] In InP capped structures, the vacancies emanating from the ion-implanted region are thus much more mobile than P interstitials and should therefore be the first defect to reach the active QD region.

V. CONCLUSION

In this work, we have used PL measurements and HAADF-STEM imaging to investigate the influence of defects emanating from phosphorus implantation damage in the InP capping layer on postgrowth thermally induced intermixing in InAs/InP QDs. It was shown that P implantation with a fluence in the $5 \times 10^{11} - 10^{14}$ cm^{-2} range induces an overall blueshifting of the PL spectra with significant bandwidth broadening even for $T_a < 600$ °C. Analysis of the QD peak evolution as a function of the level of intermixing revealed that bandwidth broadening results from the coexistence of both non- and heavily intermixed QD structures, consequential to a spatially nonuniform intermixing process. We have also investigated the atomistic mechanism driving ion-implantation-induced intermixing using a specially designed sample in which QDs are capped with compressively strained InGaAs/InP QWs to trap vacancies created by the ion-induced damage. The overall blueshift and bandwidth broadening of the spectra are suppressed in samples with strained InGaAs QWs, with the PL spectra exhibiting an evolution similar to that expected for intermixing mediated by interstitials. Based on these results, we have concluded that ion-implantation-induced intermixing in InP capped InAs/InP QDs is primarily driven by the motion of vacancies emanating from the implanted region. It was also shown that ion-implantation-induced intermixing in InAs/InP QDs produces significant modifications in the shape of the QDs, transforming them from truncated pyramids in the as-grown state to double convex lens structures. In addition, using atomistic strain calculations, these observations were found to be consistent with vacancy trapping in the vicinity of the QDs. This phenomenon is also believed to be responsible for the large degree of interdiffusion in ion-implanted samples subjected to a relatively low temperature annealing.

[1]R. Notzel, S. Anantathanasarn, R. P. J. Van Veldhoven, F. W. M. Van Otten, T. J. Eijkemans, A. Trampert, B. Satpati, Y. Barbarin, E. A. J. M. Bente, Y.-S. Oei, T. De Vries, E.-J. Geluk, B. Smalbrugge, M. K. Smit, and J. H. Wolter, Jpn. J. Appl. Phys., Part 1 **45**, 6544 (2006).
[2]G. Ortner, C. N. Allen, C. Dion, P. Barrios, D. Poitras, D. Dalacu, G.

Pakulski, J. Lapointe, P. J. Poole, W. Render, and S. Raymond, Appl. Phys. Lett. **88**, 121119 (2006).

[3] S. K. Ray, K. M. Groom, H. Y. Liu, M. Hopkinson, and R. A. Hogg, Jpn. J. Appl. Phys., Part 1 **45**, 2542 (2006).

[4] J. E. Haysom, P. J. Poole, R. L. Williams, S. Raymond, and G. C. Aers, Solid State Commun. **116**, 187 (2000).

[5] S. K. Si, D. H. Yeo, H. H. Yoon, and S. J. Kim, IEEE J. Sel. Top. Quantum Electron. **4**, 619 (1998).

[6] C. Carmody, H. H. Tan, and C. Jagadish, J. Appl. Phys. **93**, 4468 (2003).

[7] S. Charbonneau, E. S. Koteles, P. J. Poole, J. J. He, G. C. Aers, J. Haysom, M. Buchanan, Y. Feng, A. Delage, F. Yang, M. Davies, R. D. Goldberg, P. G. Piva, and I. V. Mitchell, IEEE J. Sel. Top. Quantum Electron. **4**, 772 (1998).

[8] J. E. Haysom, P. G. Piva, P. J. Poole, G. C. Aers, S. Raymond, H. Chen, R. M. Feenstra, S. Charbonneau, and I. V. Mitchell, Proceedings of the International Semiconducting and Insulating Materials Conference, 2000 (unpublished), p. 197.

[9] J. F. Girard, C. Dion, P. Desjardins, C. N. Allen, P. J. Poole, and S. Raymond, Appl. Phys. Lett. **84**, 3382 (2004).

[10] C. K. Chia, S. J. Chua, S. Tripathy, and J. R. Dong, Appl. Phys. Lett. **86**, 051905 (2005).

[11] S. Tripathy, C. K. Chia, J. R. Dong, and S. J. Chua, Electrochem. Solid-State Lett. **8**, G194 (2005).

[12] S. Barik, L. Fu, H. H. Tan, and C. Jagadish, Appl. Phys. Lett. **90**, 243114 (2007).

[13] C. Dion, P. J. Poole, S. Raymond, P. Desjardins, and F. Schiettekatte, Appl. Phys. Lett. **89**, 131905 (2006).

[14] C. Dion, P. Desjardins, M. Chicoine, F. Schiettekatte, P. J. Poole, and S. Raymond, Nanotechnology **18**, 015404 (2007).

[15] B. Salem, V. Aimez, D. Morris, A. Turala, P. Regreny, and M. Gendry, Appl. Phys. Lett. **87**, 241115 (2005).

[16] Y. C. Chen, J. Singh, and P. K. Bhattacharya, J. Appl. Phys. **74**, 3800 (1993).

[17] P. I. Gaiduk, J. L. Hansen, and A. N. Larsen, Nucl. Instrum. Methods Phys. Res. B **230**, 214 (2005).

[18] C. Dion, P. Desjardins, N. Shtinkov, F. Schiettekatte, P. J. Poole, and S. Raymond, J. Appl. Phys. **103**, 083526 (2008).

[19] D. P. Docter, J. P. Ibbetson, and Y. Gao, Proceedings of the International Conference on Indium Phosphide and Related Materials, 1998 (unpublished), p. 53.

[20] P. Dreszer, W. M. Chen, K. Seendripu, J. A. Wolk, W. Walukiewicz, B. W. Liang, C. W. Tu, and E. R. Weber, Phys. Rev. B **47**, 4111 (1993).

[21] H. Hausmann and P. Ehrhart, Phys. Rev. B **51**, 17542 (1995).

[22] K. Karsten and P. Ehrhart, Phys. Rev. B **51**, 10508 (1995).

[23] J. Groenen, G. Landa, R. Carles, P. S. Pizani, and M. Gendry, J. Appl. Phys. **82**, 803 (1997).

[24] J. F. Ziegler, J. P. Biersack, and U. Littmark, *The Stopping and Ion Range of Ions in Matter* (Pergamon, New York, 1985).

[25] M. D. Robertson, M. Burns, and T. Morrison, Microscopical Society of Canada Bulletin **33**, 19 (2006).

[26] M. D. Robertson, J. C. Bennett, A. M. Webb, J. M. Corbett, S. Raymond, and P. J. Poole, Ultramicroscopy **103**, 205 (2005).

[27] S. Raymond, S. Studenikin, S.-J. Cheng, M. Pioro-Ladriere, M. Ciorga, P. J. Poole, and M. D. Robertson, Semicond. Sci. Technol. **18**, 385 (2003).

[28] C. Dion, P. Desjardins, N. Shtinkov, M. D. Robertson, F. Schiettekatte, P. J. Poole, and S. Raymond, Phys. Rev. B **77**, 075338 (2008).

[29] P. J. Poole, J. McCaffrey, R. L. Williams, J. Lefebvre, and D. Chithrani, J. Vac. Sci. Technol. B **19**, 1467 (2001).

[30] P. J. Poole, R. L. Williams, J. Lefebvre, and S. Moisa, J. Cryst. Growth **257**, 89 (2003).

[31] H. Folliot, S. Loualiche, B. Lambert, V. Drouot, and A. LeCorre, Phys. Rev. B **58**, 10700 (1998).

[32] J. D. Eshelby, Philos. Trans. R. Soc. London, Ser. A **244**, 87 (1951).

[33] R. W. Balluffi, S. M. Allen, and W. C. Carter, *Kinetics of Materials* (Wiley, New York, 2005).

[34] D. Gershoni, H. Temkin, J. M. Vandenberg, S. N. G. Chu, R. A. Hammn, and M. B. Panish, Phys. Rev. Lett. **60**, 448 (1988).

[35] J. E. Haysom, G. C. Aers, S. Raymond, and P. J. Poole, J. Appl. Phys. **88**, 3090 (2000).

[36] J. Zhao, J. Chen, Z. C. Feng, J. L. Chen, R. Liu, and G. Xu, Thin Solid Films **498**, 179 (2006).

[37] D. Nie, T. Mei, X. H. Tang, M. K. Chin, H. S. Djie, and Y. X. Wang, J. Appl. Phys. **100**, 046103 (2006).

[38] J. Micallef, E. H. Li, and B. L. Weiss, J. Appl. Phys. **73**, 7524 (1993).

[39] L. Ouattara, A. Mikkelsen, E. Lundgren, M. Borgstrom, L. Samuelson, and W. Seifert, Nanotechnology **15**, 1701 (2004).

[40] A. Lévesque, N. Shtinkov, R. A. Masut, and P. Desjardins, Phys. Rev. Lett. **100**, 046101 (2008).

[41] P. N. Keating, Phys. Rev. **145**, 637 (1966).

[42] J. L. Martins and A. Zunger, Phys. Rev. B **30**, 6217 (1984).

[43] G. R. Liu and S. S. Q. Jerry, Semicond. Sci. Technol. **17**, 630 (2002).

[44] V.-G. Stoleru, D. Pal, and E. Towe, Physica E (Amsterdam) **15**, 131 (2002).

[45] O. M. Khreis, W. P. Gillin, and K. P. Homewood, Phys. Rev. B **55**, 15813 (1997).

[46] A. Sibille, J. Suski, and J. Le Roux, Phys. Rev. B **30**, 1119 (1984).